Jo *et al. Soft Sci* 2024;4:27
DOI: 10.20517/ss.2024.19

Soft Science

Research Article

Open Access

Unity quantum yield of InP/ZnSe/ZnS quantum dots enabled by Zn halide-derived hybrid shelling approach

Dae-Yeon Jo[#], Hyun-Min Kim[#], Goo Min Park, Donghyeok Shin, Yuri Kim, Yang-Hee Kim, Chae Woo Ryu[*], Heesun Yang[*]

Department of Materials Science and Engineering, Hongik University, Seoul 04066, Republic of Korea.
[#]Authors contributed equally.

[*]**Correspondence to:** Prof. Heesun Yang, Prof. Chae Woo Ryu, Department of Materials Science and Engineering, Hongik University, 94, Wausan-ro, Mapo-gu, Seoul 04066, Republic of Korea. E-mail: hyang@hongik.ac.kr; cryu@hongik.ac.kr

How to cite this article: Jo DY, Kim HM, Park GM, Shin D, Kim Y, Kim YH, Ryu CW, Yang H. Unity quantum yield of InP/ZnSe/ZnS quantum dots enabled by Zn halide-derived hybrid shelling approach. *Soft Sci* 2024;4:27. https://dx.doi.org/10.20517/ss.2024.19

Received: 30 Apr 2024 **First Decision:** 4 Jun 2024 **Revised:** 12 Jun 2024 **Accepted:** 21 Jun 2024 **Published:** 17 Jul 2024

Academic Editor: YongAn Huang **Copy Editor:** Pei-Yun Wang **Production Editor:** Pei-Yun Wang

Abstract

Environment-benign indium phosphide (InP) quantum dots (QDs) show great promise as visible emitters for next-generation display applications, where bright and narrow emissivity of QDs should be required toward high-efficiency, high-color reproducibility. The photoluminescence (PL) performance of InP QDs has been consistently, markedly improved, particularly owing to the exquisite synthetic control over core size homogeneity and core/shell heterostructural variation. To date, synthesis of most high-quality InP QDs has been implemented by using zinc (Zn) carboxylate as a shell precursor that unavoidably entails the formation of surface oxide on InP core. Herein, we demonstrate synthesis of superbly bright, color-pure green InP/ZnSe/ZnS QDs by exploring an innovative hybrid Zn shelling approach, where Zn halide (ZnX_2, X = Cl, Br, I) and Zn oleate are co-used as shell precursors. In the hybrid Zn shelling process, the type of ZnX_2 is found to affect the growth outcomes of ZnSe inner shell and consequent optical properties of the resulting heterostructured InP QDs. Enabled by not only the near-complete removal of the oxide layer on InP core surface through the hybrid Zn shelling process but the controlled growth rate of ZnSe inner shell, green InP/ZnSe/ZnS QDs achieve a record quantum yield (QY) up to unity along with a highly sharp linewidth of 32 nm upon growth of an optimal ZnSe shell thickness. This work affords an effective means to synthesize high-quality heterostructured InP QDs with superb emissive properties.

Keywords: InP quantum dots, hybrid zinc shelling process, ZnSe inner shell, quantum yield

INTRODUCTION

Today, colloidal quantum dots (QDs) are scientifically and industrially important nanomaterials particularly as visible emitters for post-organic light-emitting diode next-generation displays[1-4]. Besides, high compatibility of QDs with solution processing and for inorganic-organic hybridization makes them prospective candidates for flexible/stretchable display devices[5,6]. To meet the high standards of state-of-the-art display devices that require high efficiency and color gamut, bright and narrow emissivity of QDs must be achieved. Pb-containing perovskite- and CdSe-based QDs with excellent photoluminescence (PL) quantum yield (QY) (> 90%) and sharp linewidth [full-width-at-half-maximum (FWHM)] (< 20-30 nm) are considered ideal light emitters[2,7-11], but their use is strictly limited to the commercial display panels due to the environmental regulations on toxic heavy metal elements[12,13]. In this regard, visible-emissive indium phosphide (InP)-based QDs with an environmental benignity have emerged as the most promising alternative[14-18]. A primary factor that limits the optical properties of InP QDs is the incomplete surface passivation, by which unpassivated surface dangling bonds serve as the trap sites for photoexcited carriers, detrimental to the radiative recombination. In heterovalent core/shell structure of InP QDs, ZnS has been initially chosen as a shell due to its wide band gap which enables the effective confinement of charge carriers within the InP core domain[19-22]. However, PL performance of the resulting InP/ZnS QDs was often unsatisfactory mostly thanks to the considerable interfacial strain developed by a sizable InP-ZnS lattice mismatch. Placement of better lattice-matched shells, such as GaP[23-25], ZnSe[14,26], and ZnSeS[27-29], between InP and ZnS led to significant enhancements of PL figures-of-merit (i.e., QY and FWHM). The state-of-the-art heterostructured InP QDs for green and red colors displayed PL QYs of ≥ 95% and FWHMs of ca. 35 nm[30-32]. Meanwhile, single-particle measurements of InP QDs revealed the linewidth values comparable to those of CdSe QDs (< 30 nm)[30,33], suggesting there is still large room for further synthetic improvement toward sharper, brighter emissivity of InP QDs.

In a typical synthesis of InP QDs, the carboxylic acid used to generate indium carboxylate produces water through a ketonization reaction at high temperatures. This water, in turn, induces the unwanted formation of a surface oxidation product on as-synthesized InP core[34,35], which can hamper not only full passivation of core surface but uniform growth of epitaxial shell. For an effort to etch out such surface oxide species, hydrofluoric acid (HF) was directly introduced[32] or indirectly *in-situ* generated via the reaction between ZnF_2 and carboxylic acid[36] in synthesis of "red-emissive" InP/ZnSe/ZnS QDs, resulting in PL QYs of 90%-100% and FWHMs of 35-36 nm. Although the HF treatment is a useful means for the effective removal of the surface oxide layer on InP core, its highly corrosive, toxic character may become a stumbling block for eco-friendly, sustainable mass production in the future. Thus, an alternative safe synthetic method should be unearthed. Moreover, judging from no noteworthy report on the efficacy of HF treatment on "green-emissive" InP QDs, it is highly likely that HF treatment works well only to a relatively large-sized (i.e., red-emissive) core, even though its cause appears still ambiguous.

In this contribution, a new and innovative means toward synthesis of green InP/ZnSe/ZnS QDs with a unity PL QY together with a sharp emissivity is developed. The key to synthetic success involves adding zinc oleate [$Zn(OA)_2$] to the existing zinc halide (ZnX_2)-based shell growth process. We first explore the effects of different shell precursors of $Zn(OA)_2$ and ZnX_2 (X = Cl, Br, I) on growth outcomes and optical properties of the resulting heterostructured InP QDs. InP/ZnSe/ZnS QDs shelled with oxygen-free Zn precursors of ZnX_2 exhibit not only higher PL QYs (75%-89%, depending on the type of ZnX_2) but more homogeneous particle morphologies compared to those shelled with a common Zn precursor of $Zn(OA)_2$. The subsequent hybrid shelling approach, where co-use of $Zn(OA)_2$ and ZnX_2 synergically leads to the effective removal of surface oxide species on InP core, further enables synthesis of green InP QDs having PL QYs of up to 100% along with a narrow FWHM of 32 nm upon adopting an appropriate halide precursor of $ZnBr_2$ and

reaching an optimal ZnSe inner shell thickness.

EXPERIMENTAL

Synthesis of InP core QDs

Synthesis of green-emissive InP cores was conducted by mixing 0.15 mmol of indium (In) acetate, 0.125 mmol of Zn acetate, 0.5 mmol of palmitic acid, and 5 mL of 1-octadecene (ODE) in a 50 mL flask, followed by degassing at 120 °C for 60 min. Next, 0.1 mmol of tris(trimethylsilyl)phosphine [$(TMS)_3P$] diluted with 1 mL of trioctylphosphine (TOP) was injected into the mixture under flowing nitrogen. The mixture was then heated to 240 °C, and the growth of InP cores proceeded at that temperature for 10 min. The reaction was completed by cooling the InP core growth solution to room temperature and the resulting InP cores were precipitated by adding excess ethanol and redispersed in 1 mL of toluene.

Double shelling of InP core with ZnSe/ZnS based on Zn oleate or Zn halides

For Zn oleate [$Zn(OA)_2$]-based shelling, 5.0 mmol of Zn acetate, 3 mL of ODE, and 10 mmol of oleic acid (OA), and 1 mL of InP core dispersion (in toluene) were loaded in a 50 mL flask. After the toluene was fully removed through evacuation at 120 °C for 30 min, the mixture was heated to 160 °C. For ZnSe inner shelling, Se-TOP solution [1.0 mmol of selenium (Se) dissolved in 1 mL of TOP] was rapidly introduced, followed by the reaction at 300 °C for 60 min. For a sequential growth of ZnS outer shell, S-TOP solution (0.5 mmol of S dissolved in 0.5 mL of TOP) was injected, followed by the reaction at 300 °C for 60 min. The whole growth reaction was finalized by adding 0.75 mL of 1-octanethiol (OTT) and reacting at 230 °C for 60 min. After cooling to room temperature, as-synthesized QDs were collected with the addition of excess ethanol, repeatedly purified with a combined solvent of hexane/ethanol using centrifugation, and finally redispersed in hexane. In the case of Zn halides-based shelling, 5.0 mmol of Zn halide ($ZnCl_2$, $ZnBr_2$, or ZnI_2), 3 mL of ODE, and 3 mL of oleylamine (OLA), and 1 mL of InP core dispersion were loaded in a flask and the following procedures were exactly the same as above.

Double shelling of InP core with ZnSe/ZnS based on Zn halide-derived hybrid approach

First, 5.0 mmol of Zn halide ($ZnCl_2$, $ZnBr_2$, or ZnI_2), 3 mL of ODE, 3 mL of OLA, and 1 mL of InP core dispersion were loaded in a flask, followed by the same procedures as above prior to ZnSe inner shelling. For ZnSe inner shelling, Se-TOP solution (1.0 mmol of Se dissolved in 1 mL of TOP) and Zn stock solution (2.8 mmol of Zn acetate dissolved in 0.88 mL of OA and 8 mL of ODE) were rapidly injected together, followed by the reaction at 300 °C for 60 min. Then, ZnS outer shelling was conducted by injecting S-TOP solution (0.5 mmol of S dissolved in 0.5 mL of TOP) and the Zn stock solution (0.7 mmol of Zn acetate dissolved in 0.44 mL of OA and 2 mL of ODE) and reacting at 300 °C for 60 min. The subsequent procedures were the same as above. The overall synthetic procedures are illustrated in Scheme 1.

Characterization

Absorption and PL spectra of InP QDs dispersed in hexane were measured by using ultraviolet (UV)-visible spectroscopy (Shimadzu, UV-2450) and a 500 W Xe lamp-equipped spectrophotometer (PSI Co. Ltd., Darsa Pro-5200), respectively. PL QY of QDs was assessed in an integrating hemisphere with an absolute PL QY measurement system (Otsuka, QE-2000). PL decay profile of QDs in hexane dispersion was recorded using the time-correlated single-photon counting method on a spectrophotometer (Edinburgh Instruments, FS5) equipped with a picosecond pulsed laser diode (EPL-375). High-resolution transmission electron microscopy (TEM) images of QDs were obtained with a JEM-2100F (JEOL Ltd). X-ray photoelectron spectroscopic (XPS) (Thermo Scientific Inc., K-Alpha) analysis on QDs was performed to identify their surface chemical composition. Powder X-ray diffraction (XRD) with Cu Ka radiation (Rigaku, Ultima IV) was used to additionally provide information on size variation of a series of heterostructured InP QDs. ^{31}P solid-state nuclear magnetic resonance (NMR) experiments were recorded on a spectrometer (Bruker,

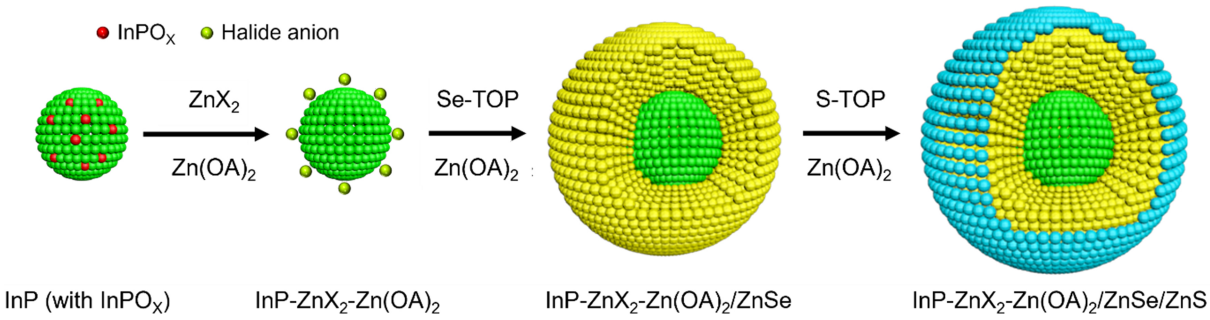

Scheme 1. Synthetic procedures from InP core to InP/ZnSe/ZnS core/shell/shell QDs. InP: Indium phosphide; QDs: quantum dots.

AVANCE II$^+$ 400 MHz NMR system). The samples were packed into 3.2 mm zirconia rotors. The rotors were spun 10 kHz at room temperature. ^{31}P solid-state NMR was performed with a recycle delay of 100 s. ^{31}P chemical shifts were referenced to an external 85% H_3PO_4 sample. Raman spectral analysis was conducted utilizing a Raman imaging microscope (Thermo Scientific Inc., DXR2xi). The samples were prepared by drop-casting the QDs solution on a silicon substrate and drying in ambient condition. All samples were excited at a wavelength of 455 nm employing a laser diode. The resultant scattering signals were captured via an electron-multiplying charge-coupled device (CCD).

RESULTS AND DISCUSSION

The present green-emissive InP cores were synthesized by heating up a mixture of $(TMS)_3P$, In acetate, Zn acetate, palmitic acid, and ODE to 240 °C, where the formed Zn carboxylate plays a role in regulating the reactivity of indium precursor with $(TMS)_3P$ via Zn-P coupling toward narrow size distribution[37-39]. The resulting InP cores displayed a well-defined absorption feature with the first excitonic peak at 440 nm along with a high valley depth (VD) of 0.4 [Supplementary Figure 1A]. The VD value, defined as the ratio of absorption between the first maximum and the minimum inflection point, is a convenient measure for assessing the size distribution particularly for binary QDs, as their band gap (E_g) variation is derived exclusively from the degree of size distribution with the compositional deviation excluded. Nemato *et al.* reported an even higher VD of 0.51 from green-emissive InP cores[40], indicating there is still room for synthetic optimization of our InP cores toward higher size homogeneity. The size of InP core required to secure green emissions of ca. 525-535 nm in PL peak wavelength typically ranges in 2-2.5 nm (corresponding to the first excitonic absorption peaks at ca. 430-460 nm), although the ultimate PL wavelength nontrivially varies with details of core/shell heterostructure including shell chemical composition and thickness. As seen in a TEM image of InP cores [Supplementary Figure 1B], the precise size determination of green-emissive InP core is highly challenging from direct microscopic measurement due to its extremely tiny size. Such size uncertainty is often tackled with the correlation between E_g versus diameter (d) (i.e., sizing curve) such as $E_g = 1.401 + 3.493/d^{1.172}$ for InP cores[41], by which the size of the present InP cores was estimated to be 2.0 nm.

InP cores were placed in a two-step shelling process, which rules out the gradual incorporation of unreacted species (yielding the non-radiative recombination channels) into the subsequent heteroepitaxial shell[42]. Distinct from the existing shelling protocol, where $Zn(OA)_2$ is exclusively used for ZnSe inner and ZnS outer shell growth, we uniquely adopted Zn halide precursors of ZnX_2 (X = Cl, Br, I). For convenience's sake, we denoted InP QDs shelled with different types of Zn precursors as InP-ZnX_2 and InP-$Zn(OA)_2$. Figure 1A presents the Zn precursor-dependent variations of PL QYs and peak wavelengths of green InP/ZnSe/ZnS QDs. InP-ZnX_2/ZnSe/ZnS QDs exhibited overall higher PL QYs (specifically, 75%-89%, depending on the type of Zn halide) compared to InP-$Zn(OA)_2$/ZnSe/ZnS ones (71%), while use of $ZnBr_2$

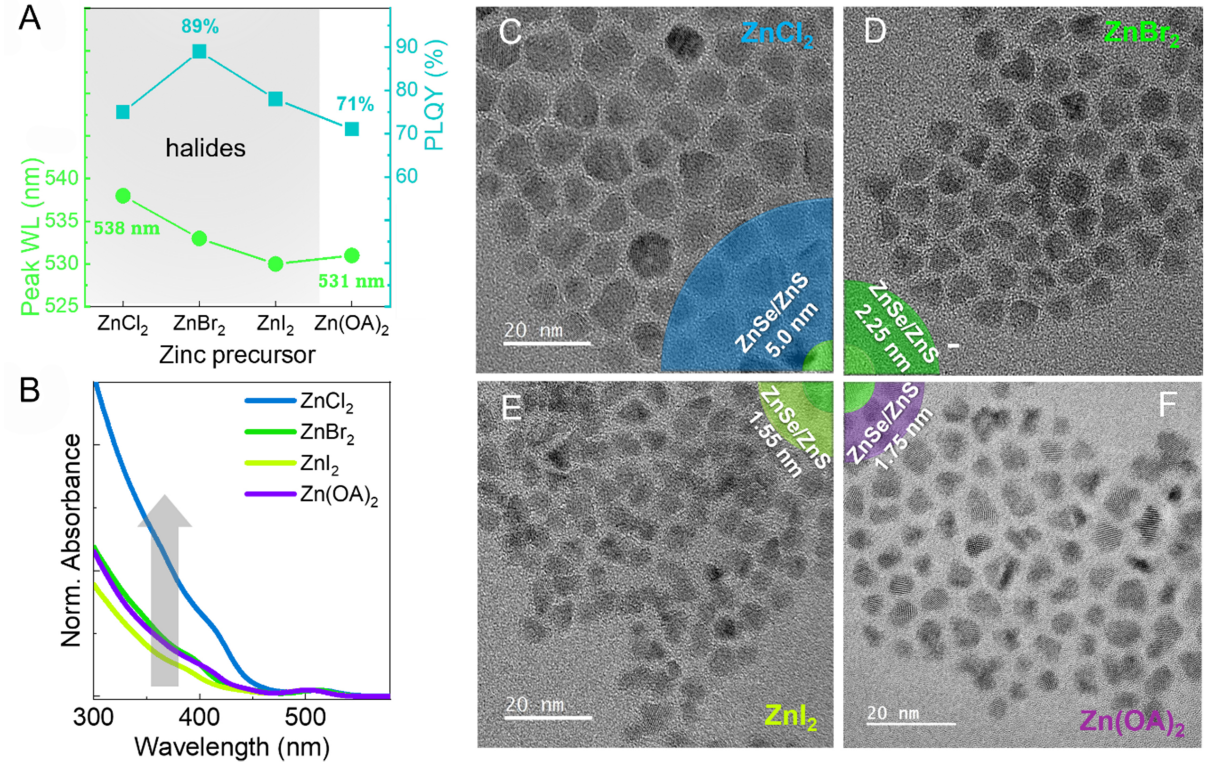

Figure 1. (A) Variations of PL QY and peak wavelength; (B) absorption spectra; and (C-F) TEM images of green InP/ZnSe/ZnS QDs synthesized with different Zn precursor types of ZnX_2 (X = Cl, Br, I) and $Zn(OA)_2$ for growth of ZnSe inner and ZnS outer shell. The double shell thicknesses of ZnSe/ZnS for individual QDs are also depicted in (C-F). The scale bars in (C-F) are all 20 nm. PL: Photoluminescence; QY: quantum yield; TEM: transmission electron microscopy; InP: indium phosphide; QDs: quantum dots.

yielded the peak value of 89%. As compared in their absorption spectra normalized at the 1S peak [Figure 1B], absorbance of InP-ZnX_2/ZnSe/ZnS QDs in blue-to-near UV region increased in the order of ZnI_2 < $ZnBr_2$ < $ZnCl_2$, while that of InP-$Zn(OA)_2$/ZnSe/ZnS QDs was slightly lower relative to InP-$ZnBr_2$/ZnSe/ZnS ones. Such a disparity in absorption is directly correlated with the thickness (or volume) of the ZnSe shell[30,43], indicative of the formation of the thickest and thinnest ZnSe shell for InP-$ZnCl_2$/ZnSe/ZnS and InP-ZnI_2/ZnSe/ZnS QDs, respectively. Being in line with the above absorption trend, the average sizes of a series of InP-ZnX_2/ZnSe/ZnS QDs systematically decreased from 10.2 [Figure 1C], 6.7 [Figure 1D] to 5.3 nm [Figure 1E] for X = Cl, Br, I, respectively, while that of InP-$Zn(OA)_2$/ZnSe/ZnS ones was 6.0 nm [Figure 1F] (refer to Supplementary Figure 2 for the respective size distribution histograms). Note that InP-ZnX_2/ZnSe/ZnS QDs overall possessed more uniform, spherical particle morphologies compared to InP-$Zn(OA)_2$/ZnSe/ZnS counterparts. Use of Zn carboxylate [e.g., $Zn(OA)_2$] as a shell precursor is well-known to entail the generation of surface $InPO_x$ during shell growth (as will be discussed later in more detail), which, in turn, renders the homogeneous growth of subsequent ZnSe shell difficult. In the case of InP/ZnSe QD heterostructure, the thickness of ZnSe shell influences the band gap (consequently, PL) primarily owing to the delocalization of electron wavefunction across the shell (which is more predominant in green-emissive core due to a relatively small conduction band offset compared to red-emissive counterpart), leading to the reduction in quantum confinement effects and consequently band gap from a thicker ZnSe shell (refer to Supplementary Figure 3A magnified from Figure 1B). On that account, as presented in normalized PL spectra of the above series of InP/ZnSe/ZnS QDs [Supplementary Figure 3B], PL peak wavelength was well proportional to ZnSe shell thickness (e.g., the longest and shortest wavelengths of 538 and 530 nm from $ZnCl_2$- and ZnI_2-based InP/ZnSe/ZnS QDs, respectively). Aligning with the above results,

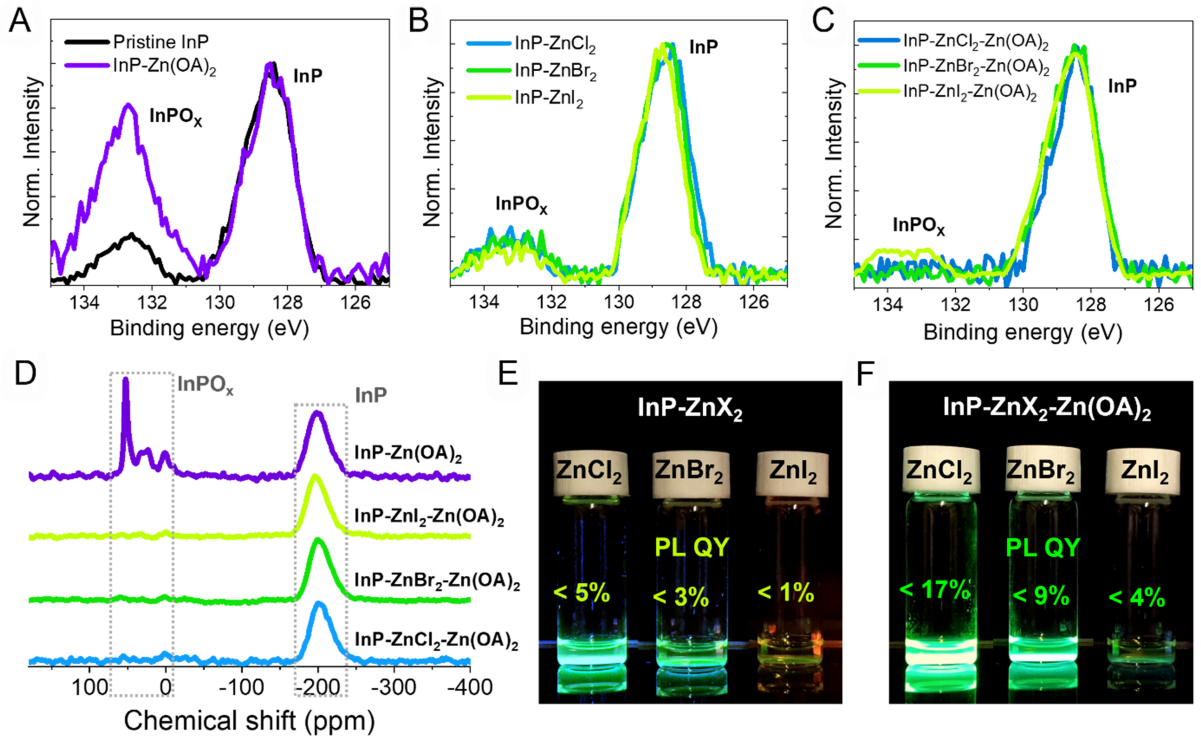

Figure 2. P 2p XPS spectra of (A) pristine InP and InP-$Zn(OA)_2$ cores; (B) a series of InP-ZnX_2 cores; and (C) a series of InP-ZnX_2-$Zn(OA)_2$ cores; (D) ^{31}P NMR spectra of InP-$Zn(OA)_2$ and a series of InP-ZnX_2-$Zn(OA)_2$ cores; Photographs of a set of (E) InP-ZnX_2 and (F) InP-ZnX_2-$Zn(OA)_2$ cores under UV irradiation. XPS: X-ray photoelectron spectroscopic; InP: indium phosphide; NMR: nuclear magnetic resonance; UV: ultraviolet.

the time-resolved PL decay profiles of the same set of InP/ZnSe/ZnS QDs showed a slower decay behavior with a thicker ZnSe shell [Supplementary Figure 3C]. We will further discuss different ZnSe shell thicknesses produced as a function of equimolar ZnX_2 later.

Surface of highly oxyphilic InP is susceptible to the oxidation. Under the synthetic environment of InP QDs in the presence of carboxylic acids, the surface oxide species (e.g., $InPO_x$) becomes easily formed by water released via the ketonization reaction ($R_1COOH + R_2COOH \rightarrow R_1COR_2 + CO_2 + H_2O$) during both core growth and subsequent shelling stage at elevated temperatures[32,36,44]. Formation of such surface oxide is well verified in the pristine InP and $Zn(OA)_2$-reacted InP core [InP-$Zn(OA)_2$] samples by an XPS analysis [Figure 2A]. The P 2p spectrum clearly shows the presence of two chemical environments for P atoms, consisting of the strong peak at 127.6-129.8 eV for InP and the weak peak at 131.7-134.1 eV for $InPO_x$. The latter peak was intensified upon an additional reaction of InP core with $Zn(OA)_2$, indicative of further promotion of $InPO_x$ formation. Meanwhile, ZnX_2-reacted InP cores (InP-ZnX_2) did not exhibit a notable change in XPS P spectrum regardless of halide type [Figure 2B] compared to pristine InP core due to the oxygen-free Zn halide sources, while the surface oxide formed during core growth still remained. For an effort to remove the remnant surface $InPO_4$, we introduced a hybrid Zn process, where the growth of ZnSe shell proceeds under co-use of ZnX_2 and $Zn(OA)_2$. Here, we denote InP core reacted with ZnX_2 and $Zn(OA)_2$ as InP-ZnX_2-$Zn(OA)_2$. We hypothesized that OA present in $Zn(OA)_2$ stock solution can participate in the reaction with co-existing ZnX_2, yielding a byproduct of hydrogen halide (HX, X = Cl, Br, I)[45]. As evident from XPS spectra of a series of InP-ZnX_2-$Zn(OA)_2$ [Figure 2C], the signal of $InPO_x$ was greatly suppressed, indicative of its effective removal, relative to the prior samples of InP-ZnX_2. These outcomes are in line with the earlier efforts to eliminate the surface oxide on "red-emissive" InP core via

direct HF[32] or ZnF_2-assisted indirect HF treatment[36]. A solid-state magic angle spinning (MAS) ^{31}P NMR is a useful tool for examining the oxidation of InP QDs as it provides the distinction between InP and $InPO_x$ (x = 2-4) along with the quantitative fraction of oxidized phosphorus[46,47]. As shown in ^{31}P NMR spectra [Figure 2D], the single peak at -200 ppm corresponds to unoxidized InP, while those between 60-0 ppm are relevant to phosphate moieties. Combined analytic results of XPS and NMR point to the effective removal of surface oxide species via adoption of a hybrid Zn process, under which HX is produced by the reaction of ZnX_2 + RCOOH → $(RCOO)_2Zn$ + 2HX and the released HX takes part in the *in-situ* etching of surface oxide. Typical PL QY of as-synthesized InP core is highly poor (i.e., less than 1%) due to the lack of passivation of surface defects[14,15,37,44]. A set of InP-ZnX_2 samples exhibited low PL QYs of 1%-5% [Figure 2E], while another set of InP-ZnX_2-$Zn(OA)_2$ ones possessed overall higher values of 4%-17% [Figure 2F], depending on the type of Zn halide. An increasing tendency in PL QY is commonly observable in the order of Cl > Br > I from both sets of samples. ZnX_2 as Z-type ligand can be involved with the passivation of undercoordinated surface P (hole trap state)[48,49]. Simultaneously, X^- ions released from ZnX_2 can also serve as X-type ligands for the passivation of undercoordinated surface In (electron trap state)[50]. The above PL QY tendency as a function of halide can be understood from the consensus that the smaller size of either ZnX_2 or X^- is more advantageous in surface passivation from a perspective of steric hindrance[50,51]. Besides, higher PL QYs of InP-ZnX_2-$Zn(OA)_2$ compared to InP-ZnX_2 samples (with the type of ZnX_2 identical) are ascribable to better ligand passivation enabled by the surface oxide removal, further validating the above analytical outcomes. Presence of surface halide species sitting on InP-ZnX_2-$Zn(OA)_2$ samples can be verified by XPS analysis [Supplementary Figure 4].

Leveraging the above hybrid Zn process, subsequent ZnSe shelling was implemented for InP-ZnX_2-$Zn(OA)_2$ by co-injecting the equimolar Se stock solution. Figure 3A-C presents TEM images of a set of InP/ZnSe QDs with use of $ZnCl_2$, $ZnBr_2$, and ZnI_2, corresponding to the average sizes of 8.0, 5.6, and 5.1 nm, respectively. This size trend is in line with that from the previous InP-ZnX_2/ZnSe/ZnS QDs [Figure 1C-E], manifesting that the thickness of ZnSe shell is sensitively dependent on the type of ZnX_2 despite use of the identical molar quantity of ZnX_2. In the case of synthesis of aminophosphine-derived InP cores, where InX_3 as a cationic precursor is used in the presence of amines such as OLA, the size of the resulting cores tends to increase in the order of Cl > Br > I[52], which is analogous to the present ZnX_2-dependent variation of ZnSe shell thickness. Based on the assumption of surface reaction-limited condition, ZnSe shell growth would be expected to be facilitated under the enhanced solute solubility and the increased rate constant of surface reaction[52]. For ZnX_2, OLA, categorized as a hard base, may be able to produce the complexes by more strongly coordinating with $ZnCl_2$ compared to ZnI_2, indicative of a higher solute solubility of the former versus the latter. Meanwhile, given the adsorption of halide on InP core surface (as evidenced from Supplementary Figure 4), the least bulky surface halide of Cl^- ions will render ZnSe shell growth easier, raising the rate of surface reaction. Disparity in ZnSe shell thickness as a function of ZnX_2 is well reflected in absorption spectra normalized at the 1S peak [Figure 3D], where a greater absorbance in blue-to-near UV region was observed in the sequence of Cl > Br > I. Accordingly, PL systematically shifted with a thicker ZnSe shell from 531 (for ZnI_2) to 539 nm (for $ZnCl_2$) [Figure 3E], being related to the ZnSe shell thickness-dependent delocalization of electron wavefunction aforementioned. Even without ZnS outer shelling, PL QYs of a series of InP/ZnSe QDs were relatively high. In InP-ZnX_2-$Zn(OA)_2$/ZnSe QDs $ZnBr_2$ yielded the highest PL QY of 93%, while $ZnCl_2$ and ZnI_2 gave comparable values of 83%-85% [Figure 3F]. As argued above, use of $ZnCl_2$ leads to the fastest ZnSe shell growth, which stochastically renders controlled heteroepitaxial shell growth unlikely, thus leaving some imperfect sites at hetero-interface and/or shell interior. As an opposite case, the introduction of ZnI_2 induces the slowest shell growth reaction entailing the formation of the thinnest ZnSe shell, which can often encounter the high probability of incomplete shell coverage on core surface. Besides, HI is known as an unstable chemical as it spontaneously oxidizes to molecular iodine (I_2) during the reaction[53,54], implying that in removing the surface oxide, it may not serve

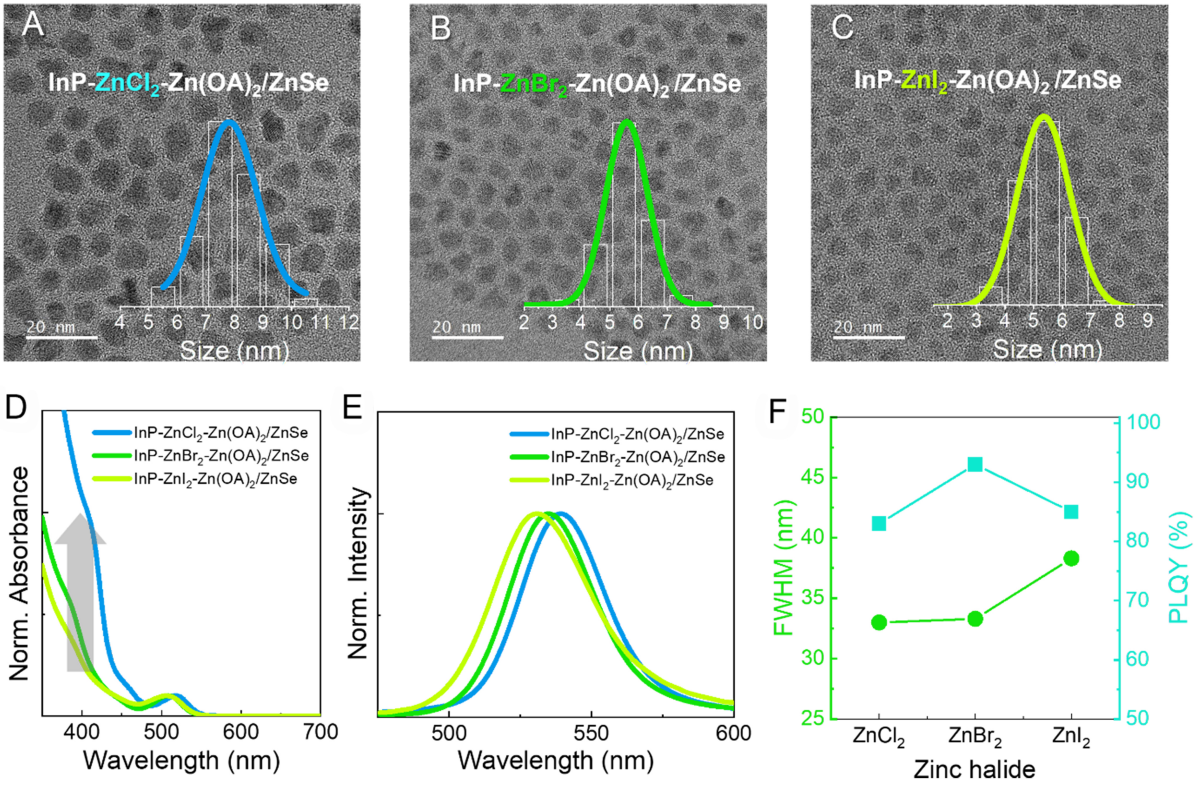

Figure 3. (A-C) TEM images and size distribution histograms (insets); (D) absorption spectra normalized at the 1S peak; (E) normalized PL spectra; and (F) variations of FWHM and PL QY of a series of InP-ZnX_2-$Zn(OA)_2$/ZnSe QDs. TEM: Transmission electron microscopy; PL: photoluminescence; FWHM: full-width-at-half-maximum; QY: quantum yield; InP: indium phosphide; QDs: quantum dots.

as a perfect reagent (*vs.* HCl and HBr), leaving unetched $InPO_x$ residue. This scenario may be supported by a marginal XPS signal trace of $InPO_x$ from InP-ZnI_2-$Zn(OA)_2$ unlike other two samples [Figure 2C]. In this context, $ZnBr_2$ is regarded as an optimal halide as it allows for not only the relevant ZnSe growth rate but the near-complete removal of surface oxide, synergically rendering the heteroepitaxial shell growth perfect. Meanwhile, InP-ZnX_2-$Zn(OA)_2$/ZnSe QDs with $ZnCl_2$ and $ZnBr_2$ exhibited nearly the same PL FWHM of 32 nm, while a markedly broad value of 37 nm resulted from InP-ZnI_2-$Zn(OA)_2$/ZnSe ones [Figure 3F]. Given the identical InP core, the major determinants of PL linewidth of InP/ZnSe QDs are the average thickness and thickness uniformity of ZnSe shell. As noticed from size distributions [Figure 3A-C], InP-$ZnCl_2$-$Zn(OA)_2$/ZnSe QDs possessed a relatively wide size distribution, i.e., lack of shell thickness uniformity over individual QDs (resulting from an uncontrollably fast shell growth rate), when compared to other two samples. Nevertheless, a sharp linewidth of InP-$ZnCl_2$-$Zn(OA)_2$/ZnSe QDs benefits from a sufficiently thick ZnSe, which, in turn, can mitigate the exciton-phonon coupling strength via the increasing delocalization of charge carriers[55]. A broad linewidth of InP-ZnI_2-$Zn(OA)_2$/ZnSe QDs is likely ascribable to the combined consequence of comparatively thin shell thickness and imperfect heteroepitaxial shell growth (aforementioned), both of which have unfavorable effects on the reduction of exciton-phonon coupling strength. Subsequent growth of the ZnS outer shell, for which the equimolar $Zn(OA)_2$ and S-TOP were identically used, on a series of InP-ZnX_2-$Zn(OA)_2$/ZnSe heterostructures above further boosted PL QY to 89%-100%, depending on the type of ZnX_2, while emission linewidths stayed the same [Figure 4]. Also refer to Supplementary Figure 5 for the reproducible results of unity PL QYs from the representative three InP-$ZnBr_2$-$Zn(OA)_2$/ZnSe/ZnS QD samples. Such superb emissive figures-of-merit possessing a narrow FWHM

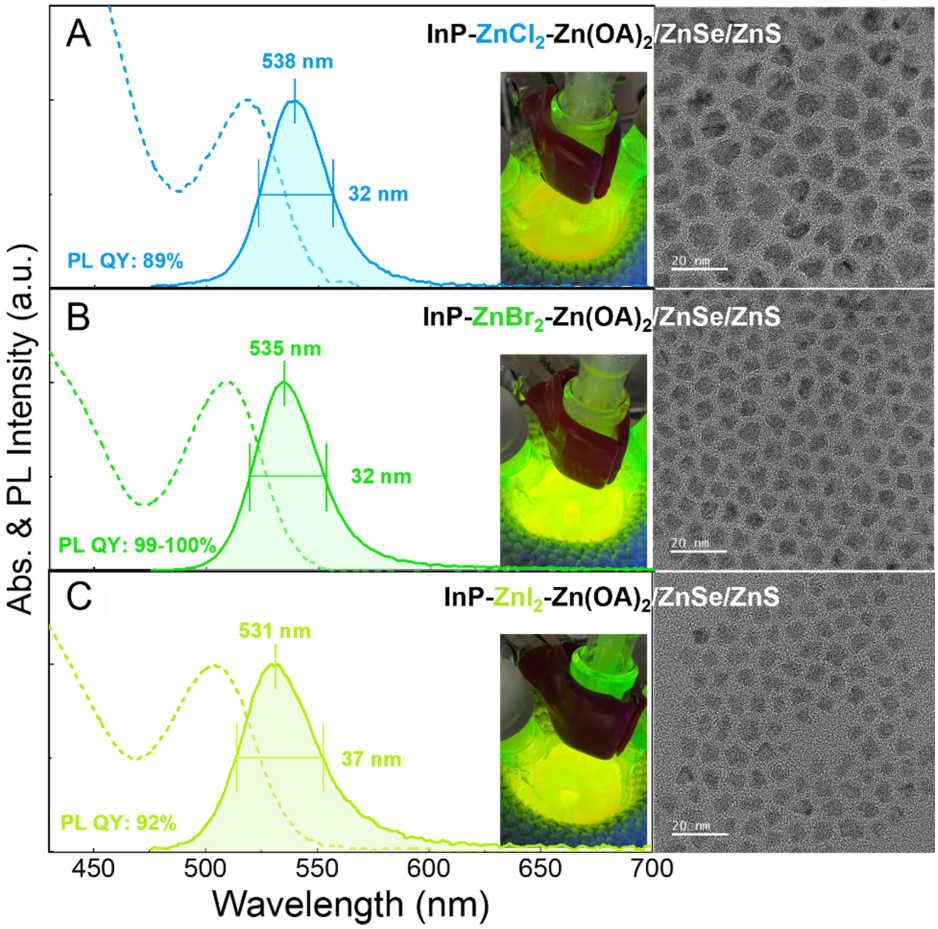

Figure 4. Absorption, PL spectra, UV-irradiated fluorescent images (insets) and TEM images (scale bar: 20 nm) of a series of InP-ZnX_2-$Zn(OA)_2$/ZnSe/ZnS QDs, where ZnX_2 is (A) $ZnCl_2$, (B) $ZnBr_2$, and (C) ZnI_2. PL: Photoluminescence; UV: ultraviolet; TEM: transmission electron microscopy; InP: indium phosphide; QDs: quantum dots.

(32 nm) and a unity PL QY of InP-$ZnBr_2$-$Zn(OA)_2$/ZnSe/ZnS QDs are definitely record values among green-emissive InP ones to date. The average sizes of InP-ZnX_2-$Zn(OA)_2$/ZnSe/ZnS QDs were 9.2, 6.4, and 5.7 nm for $ZnCl_2$, $ZnBr_2$, and ZnI_2, respectively (refer to Supplementary Figure 6 for the respective size distribution histograms and Supplementary Figure 7 for the corresponding XRD patterns, where the heteroepitaxial coherent reflection peaks became gradually broader from $ZnCl_2$, $ZnBr_2$ to ZnI_2), and thus, the average ZnS shell thicknesses were estimated to be 0.6, 0.4, and 0.3 nm, respectively. The thickness trend in ZnS shell also aligns with that in ZnSe shell [Figure 3A-C], implying that the growth kinetics of ZnS shell depends on the type of halides remaining after ZnSe shelling in a similar manner to that of ZnSe shell.

Lastly, based on the best-performing InP-$ZnBr_2$-$Zn(OA)_2$/ZnSe/ZnS QDs, the thickness of ZnSe inner shell was further modulated simply by proportionally varying the respective amounts of Se-TOP (specifically, 0.5, 1.0, and 1.5 mmol) and $Zn(OA)_2$ (specifically, 1.4, 2.8, and 4.2 mmol) injected for ZnSe shelling and the resulting inner shell is denoted as thin-, medium-, and thick-ZnSe for convenience's sake. Also note that the above InP-$ZnBr_2$-$Zn(OA)_2$/ZnSe/ZnS QDs in Figure 4B correspond to medium-ZnSe having a ZnSe shell thickness (t_{ZnSe}) of 1.8 nm. With increasing thickness of ZnSe inner shell, the sizes increased from 3.9 to 6.4 nm for InP/ZnSe [Supplementary Figure 8] (corresponding to the t_{ZnSe} of 1.0 to 2.2 nm, respectively) and from 4.5 to 7.0 nm for InP/ZnSe/ZnS QDs [Figure 5A and B]. Systematically augmented absorbance of InP/

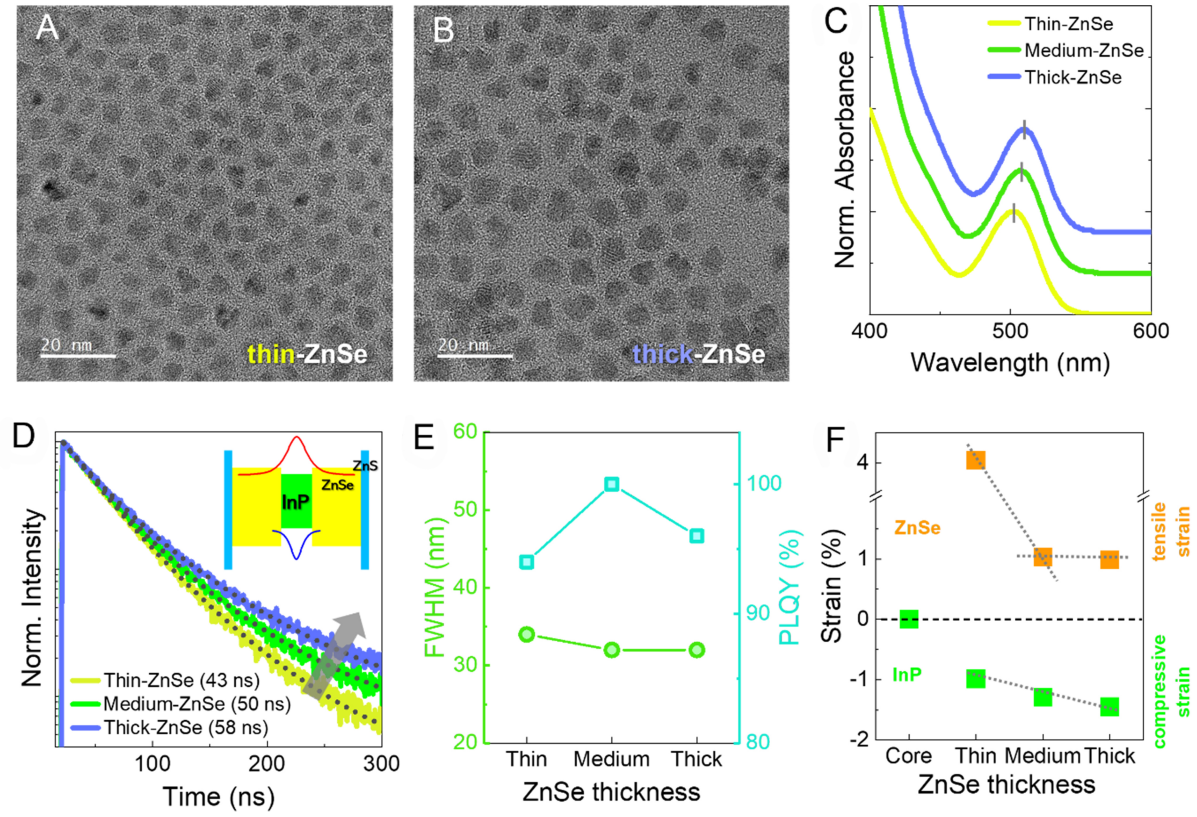

Figure 5. TEM images (scale bar: 20 nm) of InP-$ZnBr_2$-$Zn(OA)_2$/ZnSe/ZnS QDs having (A) thin- and (B) thick-ZnSe; (C) Absorption spectra; (D) time-resolved PL decay profiles; (E) variations of FWHM and PL QY of InP-$ZnBr_2$-$Zn(OA)_2$/ZnSe/ZnS QDs as a function of ZnSe shell thickness; (F) ZnSe shell thickness-dependent change of heterostructural strain of InP core and ZnSe shell of InP-$ZnBr_2$-$Zn(OA)_2$/ZnSe QDs. TEM: Transmission electron microscopy; InP: indium phosphide; QDs: quantum dots; PL: photoluminescence; FWHM: full-width-at-half-maximum; QY: quantum yield.

ZnSe/ZnS QDs in blue-to-near UV region from thin-ZnSe to thick-ZnSe [Supplementary Figure 9] is attributable to the increasing volume of ZnSe shell (as stated earlier). Spectral redshift in 1S excitonic absorption peak from 501 to 510 nm [Figure 5C] and gradually lengthened decaying behavior from 43 to 58 ns in average lifetime (τ_{avg}) [Figure 5D] also result from an increasing delocalization of electron wavefunction with a thicker ZnSe shell. While InP/ZnSe/ZnS QDs possessed a peak PL QY (99%-100%) from medium-ZnSe, those consisting of thin- and thick-ZnSe yielded lower values (94%-96%). Meanwhile, PL linewidth (34 nm) of thin-ZnSe-based QDs was somewhat broader compared to that (32 nm) of medium- and thick-ZnSe-based ones [Figure 5E], being associated with the ZnSe inner shell thickness-dependent exciton-phonon coupling strength aforementioned. The above trend in PL QY indicates that the critical ZnSe inner shell thickness lies in the proximity of 1.8 nm (i.e., medium-ZnSe), above which the heterostructural strain becomes nontrivial, likely generating the incoherent lattice defects from the strain relaxation[56]. To examine ZnSe inner shell thickness-dependent strain behavior, Raman spectroscopic analysis was performed on InP-$ZnBr_2$-$Zn(OA)_2$/ZnSe QDs. Given the lattice mismatch (3.4%) between InP (5.86 Å) and ZnSe (5.66 Å), InP core and ZnSe shell are placed under a compressive and tensile strain, respectively. The degree of deformation can be evaluated by the frequency change of the longitudinal optical (LO) phonon of InP core caused by the overgrowth of ZnSe inner shell. In the heterostructure, the LO mode of compressively strained InP core (having a reduced interatomic spacing) shifts to a higher frequency, while ZnSe under a tensile strain (rendering the interatomic spacing expanded) exhibits the shift of LO frequency in the opposite direction. Supplementary Figure 10 depicts Raman spectral evolution of

InP core and a series of InP/ZnSe QDs with varying ZnSe shell thicknesses. Figure 5F summarizes the strain results of InP core and InP/ZnSe QDs obtained by Raman spectroscopic analysis [Supplementary Materials]. For InP/thin-ZnSe, ZnSe shell undergoes a high degree of tensile strain, suggesting that it may form in the manner of somewhat partially island-shaped growth[57]. Upon growth to medium-ZnSe, the tensile strain becomes substantially relieved, indicating the formation of the coherent ZnSe shell with complete coverage. In the case of InP/thick-ZnSe, the strain is further reduced, albeit slightly, due to the continuing growth of ZnSe shell in the thermodynamically stable direction. Meanwhile, the compressive strain of InP core consistently increases with a thicker growth of ZnSe shell. Judging from the above strain analysis, the excessive compressive strain imposed on InP core by the growth of a thick-ZnSe shell (exceeding a critical thickness) likely gives rise to the generation of interfacial defect and/or misfit dislocation, thus entailing a decline of PL QY.

CONCLUSIONS

In green-emissive heterostructured InP QDs, the effects of the type of Zn precursor for shelling on shell growth outcomes and consequent optical properties were investigated. When Zn halides were used for shelling, the resulting InP/ZnSe/ZnS QDs overall possessed not only more uniform, spherical particle morphologies but higher PL QYs compared to those shelled with the conventional Zn precursor of $Zn(OA)_2$, benefiting from oxygen-free halide precursors that can suppress the formation of surface oxide during shell growth. For an effort to remove the remnant surface oxide generated during core growth, a hybrid Zn shelling process, where Zn halide and $Zn(OA)_2$ were co-used as shell sources, was newly devised. Our hypothesis that the surface oxide species can be effectively *in-situ* etched by a byproduct of hydrogen halide released via the reaction of $Zn(OA)_2$ with co-existing ZnX_2, was supported by the combined analytic results of XPS and NMR. The growth rate and consequent thickness of ZnSe inner shell were sensitively dependent on the type of ZnX_2 in the hybrid Zn shelling process, showing the increasing thickness in the order of $ZnCl_2$ > $ZnBr_2$ > ZnI_2 (which was also rationalized with respect to the solute solubility and rate constant of surface reaction). Among ZnX_2 used, $ZnBr_2$ was found to be an ideal halide as it enabled not only the relevant ZnSe growth rate but the near-complete removal of the surface oxide. Upon ZnS outer shelling on $ZnBr_2$-based InP/ZnSe QDs with an optimal ZnSe shell thickness, the resulting green QDs produced a record PL QY of unity together with a sharp linewidth of 32 nm.

DECLARATIONS

Authors' contributions

Made substantial contributions to the conception and design of the study: Yang H, Ryu CW, Jo DY
Performed data analysis and interpretation and wrote the manuscript: Jo DY, Kim HM, Ryu CW, Yang H
Provided administrative, technical, and material support: Park GM, Shin D, Kim Y, Kim YH

Availability of data and materials

Not applicable.

Financial support and sponsorship

This research was supported by the National Research Foundation of Korea (NRF) grant funded by the Korean government (MSIT) (RS-2024-00411892, 2020M3H4A3082656) and the Technology Innovation Program (20010737, 20016332) funded by the Ministry of Trade, Industry & Energy (MOTIE, Korea). This work was also supported by the 2023 Hongik University Research Fund.

Conflicts of interest

All authors declared that there are no conflicts of interest.

Ethical approval and consent to participate

Not applicable.

Consent for publication

Not applicable.

REFERENCES

1. Pietryga JM, Park YS, Lim J, et al. Spectroscopic and device aspects of nanocrystal quantum dots. *Chem Rev* 2016;116:10513-622. DOI PubMed
2. Yang Z, Gao M, Wu W, et al. Recent advances in quantum dot-based light-emitting devices: challenges and possible solutions. *Mater Today* 2019;24:69-93. DOI
3. Dai X, Deng Y, Peng X, Jin Y. Quantum-dot light-emitting diodes for large-area displays: towards the dawn of commercialization. *Adv Mater* 2017;29:1607022. DOI PubMed
4. Han C, Yang H. Development of colloidal quantum dots for electrically driven light-emitting devices. *J Korean Ceram Soc* 2017;54:449-69. DOI
5. Lin Q, Zhu Y, Wang Y, et al. Flexible quantum dot light-emitting device for emerging multifunctional and smart applications. *Adv Mater* 2023;35:e2210385. DOI PubMed
6. Kim DC, Seung H, Yoo J, et al. Intrinsically stretchable quantum dot light-emitting diodes. *Nat Electron* 2024;7:365-74. DOI
7. Bourzac K. Quantum dots go on display. *Nature* 2013;493:283. DOI PubMed
8. Mashford BS, Stevenson M, Popovic Z, et al. High-efficiency quantum-dot light-emitting devices with enhanced charge injection. *Nature Photon* 2013;7:407-12. DOI
9. Lu M, Zhang Y, Wang S, Guo J, Yu WW, Rogach AL. Metal halide perovskite light-emitting devices: promising technology for next-generation displays. *Adv Funct Mater* 2019;29:1902008. DOI
10. Chen O, Zhao J, Chauhan VP, et al. Compact high-quality CdSe-CdS core-shell nanocrystals with narrow emission linewidths and suppressed blinking. *Nat Mater* 2013;12:445-51. DOI PubMed PMC
11. Hu S, Shabani F, Liu B, et al. High-performance deep red colloidal quantum well light-emitting diodes enabled by the understanding of charge dynamics. *ACS Nano* 2022;16:10840-51. DOI PubMed
12. Yang SJ, Oh JH, Kim S, Yang H, Do YR. Realization of InP/ZnS quantum dots for green, amber and red down-converted LEDs and their color-tunable, four-package white LEDs. *J Mater Chem C* 2015;3:3582-91. DOI
13. Liu P, Lou Y, Ding S, et al. Green InP/ZnSeS/ZnS core multi-shelled quantum dots synthesized with aminophosphine for effective display applications. *Adv Funct Mater* 2021;31:2008453. DOI
14. Ramasamy P, Kim N, Kang Y, Ramirez O, Lee J. Tunable, bright, and narrow-band luminescence from colloidal indium phosphide quantum dots. *Chem Mater* 2017;29:6893-9. DOI
15. Cao F, Wang S, Wang F, Wu Q, Zhao D, Yang X. A layer-by-layer growth strategy for large-size InP/ZnSe/ZnS core–shell quantum dots enabling high-efficiency light-emitting diodes. *Chem Mater* 2018;30:8002-7. DOI
16. Tamang S, Lincheneau C, Hermans Y, Jeong S, Reiss P. Chemistry of InP nanocrystal syntheses. *Chem Mater* 2016;28:2491-506. DOI
17. Song W, Lee S, Yang H. Fabrication of warm, high CRI white LED using non-cadmium quantum dots. *Opt Mater Express* 2013;3:1468. DOI
18. Kim K, Jo J, Jo D, et al. Cation-exchange-derived InGaP alloy quantum dots toward blue emissivity. *Chem Mater* 2020;32:3537-44. DOI
19. Lad AD, Mahamuni S. Effect of ZnS shell formation on the confined energy levels of ZnSe quantum dots. *Phys Rev B* 2008;78:125421. DOI
20. Li Z, Wei J, Wang F, et al. Carrier dynamics in alloyed chalcogenide quantum dots and their light-emitting devices. *Adv Energy Mater* 2021;11:2101693. DOI
21. Li L, Reiss P. One-pot synthesis of highly luminescent InP/ZnS nanocrystals without precursor injection. *J Am Chem Soc* 2008;130:11588-9. DOI PubMed
22. Ryu E, Kim S, Jang E, et al. Step-wise synthesis of InP/ZnS core−shell quantum dots and the role of zinc acetate. *Chem Mater* 2009;21:573-5. DOI
23. Kim S, Kim T, Kang M, et al. Highly luminescent InP/GaP/ZnS nanocrystals and their application to white light-emitting diodes. *J Am Chem Soc* 2012;134:3804-9. DOI PubMed
24. Park JP, Lee JJ, Kim SW. Highly luminescent InP/GaP/ZnS QDs emitting in the entire color range via a heating up process. *Sci Rep* 2016;6:30094. DOI PubMed PMC
25. Xu Y, Lv Y, Wu R, et al. Preparation of highly stable and photoluminescent cadmium-free InP/GaP/ZnS core/shell quantum dots and

application to quantitative immunoassay. *Part Part Syst Char* 2020;37:1900441. DOI

26. Li Y, Hou X, Dai X, et al. Stoichiometry-controlled InP-based quantum dots: synthesis, photoluminescence, and electroluminescence. *J Am Chem Soc* 2019;141:6448-52. DOI PubMed
27. Lim J, Bae WK, Lee D, et al. InP@ZnSeS, core@composition gradient shell quantum dots with enhanced stability. *Chem Mater* 2011;23:4459-63. DOI
28. Hahm D, Chang JH, Jeong BG, et al. Design principle for bright, robust, and color-pure InP/$ZnSe_xS_{1-x}$/ZnS heterostructures. *Chem Mater* 2019;31:3476-84. DOI
29. Jo J, Jo D, Lee S, et al. InP-based quantum dots having an InP core, composition-gradient ZnSeS inner shell, and ZnS outer shell with sharp, bright emissivity, and blue absorptivity for display devices. *ACS Appl Nano Mater* 2020;3:1972-80. DOI
30. Lee SH, Kim Y, Jang H, et al. The effects of discrete and gradient mid-shell structures on the photoluminescence of single InP quantum dots. *Nanoscale* 2019;11:23251-8. DOI PubMed
31. Kim Y, Ham S, Jang H, et al. Bright and uniform green light emitting InP/ZnSe/ZnS quantum dots for wide color gamut displays. *ACS Appl Nano Mater* 2019;2:1496-504. DOI
32. Won YH, Cho O, Kim T, et al. Highly efficient and stable InP/ZnSe/ZnS quantum dot light-emitting diodes. *Nature* 2019;575:634-8. DOI PubMed
33. Cui J, Beyler AP, Marshall LF, et al. Direct probe of spectral inhomogeneity reveals synthetic tunability of single-nanocrystal spectral linewidths. *Nat Chem* 2013;5:602-6. DOI PubMed PMC
34. Cros-Gagneux A, Delpech F, Nayral C, Cornejo A, Coppel Y, Chaudret B. Surface chemistry of InP quantum dots: a comprehensive study. *J Am Chem Soc* 2010;132:18147-57. DOI PubMed
35. Choi S, Kim H, Yoon S, et al. Aminophosphine-derived, high-quality red-emissive InP quantum dots by the use of an unconventional in halide. *J Mater Chem C* 2022;10:2213-22. DOI
36. Li H, Zhang W, Bian Y, Ahn TK, Shen H, Ji B. ZnF_2-assisted synthesis of highly luminescent InP/ZnSe/ZnS quantum dots for efficient and stable electroluminescence. *Nano Lett* 2022;22:4067-73. DOI PubMed
37. Xi L, Cho DY, Besmehn A, et al. Effect of zinc incorporation on the performance of red light emitting InP core nanocrystals. *Inorg Chem* 2016;55:8381-6. DOI PubMed
38. Koh S, Eom T, Kim WD, et al. Zinc–phosphorus complex working as an atomic valve for colloidal growth of monodisperse indium phosphide quantum dots. *Chem Mater* 2017;29:6346-55. DOI
39. Kim K, Suh Y, Kim D, et al. Zinc oxo clusters improve the optoelectronic properties on indium phosphide quantum dots. *Chem Mater* 2020;32:2795-802. DOI
40. Nemoto K, Watanabe J, Sun HT, Shirahata N. Coherent InP/ZnS core@shell quantum dots with narrow-band green emissions. *Nanoscale* 2022;14:9900-9. DOI PubMed
41. Cho E, Jang H, Lee J, Jang E. Modeling on the size dependent properties of InP quantum dots: a hybrid functional study. *Nanotechnology* 2013;24:215201. DOI PubMed
42. Taylor DA, Teku JA, Cho S, Chae W, Jeong S, Lee J. Importance of surface functionalization and purification for narrow FWHM and bright green-emitting InP core–multishell quantum dots via a two-step growth process. *Chem Mater* 2021;33:4399-407. DOI
43. Jo J, Jo D, Choi S, et al. Highly bright, narrow emissivity of InP quantum dots synthesized by aminophosphine: effects of double shelling scheme and Ga treatment. *Adv Opt Mater* 2021;9:2100427. DOI
44. Kim TG, Zherebetskyy D, Bekenstein Y, et al. Trap passivation in indium-based quantum dots through surface fluorination: mechanism and applications. *ACS Nano* 2018;12:11529-40. DOI PubMed
45. Xu S, Ziegler J, Nann T. Rapid synthesis of highly luminescent InP and InP/ZnS nanocrystals. *J Mater Chem* 2008;18:2653. DOI
46. Tessier MD, Baquero EA, Dupont D, et al. Interfacial oxidation and photoluminescence of InP-based core/shell quantum dots. *Chem Mater* 2018;30:6877-83. DOI
47. Ubbink RF, Almeida G, Iziyi H, et al. A water-free in situ HF treatment for ultrabright InP quantum dots. *Chem Mater* 2022;34:10093-103. DOI PubMed PMC
48. Anderson NC, Hendricks MP, Choi JJ, Owen JS. Ligand exchange and the stoichiometry of metal chalcogenide nanocrystals: spectroscopic observation of facile metal-carboxylate displacement and binding. *J Am Chem Soc* 2013;135:18536-48. DOI PubMed PMC
49. Kirkwood N, Monchen JOV, Crisp RW, et al. Finding and fixing traps in II-VI and III-V colloidal quantum dots: the importance of Z-type ligand passivation. *J Am Chem Soc* 2018;140:15712-23. DOI PubMed PMC
50. Purcell-milton F, Chiffoleau M, Gun'ko YK. Investigation of quantum dot–metal halide interactions and their effects on optical properties. *J Phys Chem C* 2018;122:25075-84. DOI
51. Calvin JJ, Swabeck JK, Sedlak AB, Kim Y, Jang E, Alivisatos AP. Thermodynamic investigation of increased luminescence in indium phosphide quantum dots by treatment with metal halide salts. *J Am Chem Soc* 2020;142:18897-906. DOI PubMed
52. Tessier MD, Dupont D, De Nolf K, De Roo J, Hens Z. Economic and size-tunable synthesis of InP/ZnE (E = S, Se) colloidal quantum dots. *Chem Mater* 2015;27:4893-8. DOI
53. Zhu Y, Shen C, Xu X, et al. Photoluminescence properties of InP/GaP/ZnS core/shell/shell colloidal quantum dots treated with halogen acids. *J Lumin* 2023;256:119651. DOI
54. Jun B, Lee HK, Park Y, Kwon Y. Degradation of full aromatic polyamide NF membrane by sulfuric acid and hydrogen halides: change of the surface/permeability properties. *Polym Degrad Stabil* 2019;162:1-11. DOI

55. Park J, Won YH, Kim T, Jang E, Kim D. Electrochemical charging effect on the optical properties of InP/ZnSe/ZnS quantum dots. *Small* 2020;16:e2003542. DOI PubMed
56. Li H, Bian Y, Zhang W, et al. High performance InP-based quantum dot light-emitting diodes via the suppression of field-enhanced electron delocalization. *Adv Funct Mater* 2022;32:2204529. DOI
57. Van Avermaet H, Schiettecatte P, Hinz S, et al. Full-spectrum InP-based quantum dots with near-unity photoluminescence quantum efficiency. *ACS Nano* 2022;16:9701-12. DOI PubMed